Acta Astronautica 246 (2026) 19–31

Contents lists available at ScienceDirect

Acta Astronautica

journal homepage: www.elsevier.com/locate/actaastro

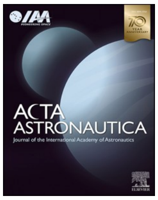

Investigation of size, mass, and area-to-mass distributions in carbon-fiber-reinforced composite panels fragments from hypervelocity impacts

Francesco Fabri [a,*], Lorenzo Olivieri [b]

[a] CISAS "G. Colombo", University of Padova, Via Venezia 1, 35131, Padova, Italy
[b] DII/CISAS, University of Padova, Via Venezia 1, 35131, Padova, Italy

ARTICLE INFO

Keywords:
Hypervelocity impact testing
Fragments distribution
Space debris
CFRP

ABSTRACT

In the next decades, hypervelocity impacts between space objects are expected to increase in frequency due to the continuous growth of the orbital debris population and the deployment of large satellite constellations. Accurate characterization of fragment physical properties is therefore essential for the development and validation of breakup models and for the modelling of the debris environment, particularly in view of the increasing use of composite materials in spacecraft structures. In this work, fragments generated by four hypervelocity impacts on carbon-fiber-reinforced polymer (CFRP) panels are experimentally analysed with the aim of investigating size, mass, and area-to-mass (A/m) distributions. In these tests, aluminium spheres (1.9 mm and 2.9 mm diameter) impacted 4 mm thick CFRP plates at velocities between 3.5 km/s and 5.1 km/s, under conditions exceeding the ballistic limit.

Fragments were individually catalogued through three-dimensional geometric measurements and mass determination, enabling the derivation of cumulative characteristic length distributions, mass–size correlations, and A/m distributions. Results show that fragment populations are strongly influenced by projectile diameter, with larger projectiles generating larger and more massive fragments, while smaller projectiles predominantly produce lighter debris. The mass-size scaling exhibits sub-quadratic behaviour, suggesting that fragment mass tends to increase more slowly than projected area with characteristic length, leading to increasing A/m values for larger fragments. Overall, the results provide a comprehensive three-dimensional experimental dataset for CFRP fragmentation and support the refinement of breakup models and debris environment simulations for composite spacecraft structures.

Nomenclature

a	Largest size
a_1, a_2	Piecewise linear fit slopes
A	Cross-sectional area
A/m	Area-to-Mass ratio
b	Intermediate size
b_1, b_2	Piecewise linear fit intercepts
c	Smallest size
L_c	Characteristic length
M	Mass
N	Total number
$RMSE$	Root Mean Squared Error

1. Introduction

The continuous growth of the orbital debris population represents one of the most critical challenges for the long-term sustainability of space activities. Current environment models estimate the presence of tens of thousands of catalogued objects larger than 10 cm, hundreds of thousands of fragments in the centimetre size range, and hundreds of millions of millimetre and sub-millimetre sized debris pieces orbiting the Earth [1,2]. While only the largest objects are routinely tracked by ground-based surveillance systems, smaller fragments remain largely unobservable despite their ability to cause severe damage due to their high relative velocities, typically exceeding 7 km/s in low Earth orbit [3–5]. The rapid increase in launch rates, driven by the deployment of

---

* Corresponding author.
E-mail address: francesco.fabri@studenti.unipd.it (F. Fabri).

https://doi.org/10.1016/j.actaastro.2026.03.061
Received 12 February 2026; Received in revised form 28 March 2026; Accepted 30 March 2026

large satellite constellations, is expected to further raise the frequency of hypervelocity collisions in the coming decades [6–8], increasing concerns about self-sustaining fragmentation cascades, first theorized by Kessler and Cour-Palais [1].

Accurate modelling of collision induced debris clouds is therefore essential for collision risk assessment, spacecraft design, and the development of effective debris mitigation strategies. In this context, international efforts coordinated by the Inter-Agency Space Debris Coordination Committee (IADC) have highlighted the importance of continuously refining long-term environment models and breakup simulations [9–13]. The reliability of these tools strongly depends on the availability and quality of empirical datasets obtained from hypervelocity impact experiments, which are used to calibrate and validate fragmentation models such as the NASA Standard Breakup Model [10]. Despite decades of experimental research, significant limitations persist in existing databases, particularly with respect to the three-dimensional characterization of fragments (e.g. thickness), as well as associated physical properties such as mass and area-to-mass ratio (A/m), which play a crucial role in determining the orbital lifetime of small debris.

Over the years, several experimental campaigns have contributed to the understanding of fragmentation physics under hypervelocity impact conditions. Large-scale experiments such as the SOCIT series and the DebriSat project provided valuable insight into catastrophic satellite breakup and fragment populations down to the millimetre scale [11–13]. Other studies focused on simplified spacecraft components, including panels and plate-like targets, in order to isolate the effects of material properties, impact velocity, and geometric parameters on fragment generation [14,15]. In particular, Nishida and co-workers performed an extensive series of hypervelocity impact experiments on both aluminium and composite targets, systematically investigating fragment size distributions as a function of projectile diameter, impact velocity, impact angle, and irradiation effects [16–19].

In parallel with the evolution of fragmentation modelling, the increasing use of advanced materials in spacecraft structures has introduced additional complexity in debris generation mechanisms. Carbon fiber reinforced polymer (CFRP) composites are now widely employed in satellite structures, partially replacing traditional aluminium alloys due to their high specific stiffness and strength. However, the layered architecture and anisotropic mechanical behaviour of CFRPs significantly influence their response to hypervelocity impacts, affecting damage morphology, crack propagation, and fragment generation mechanisms [20,21]. Experimental evidence suggests that fragment populations generated from CFRP targets can differ substantially from those produced by isotropic metallic materials, both in terms of size distribution and fragment morphology [16,22]. Despite this, available experimental data on CFRP fragmentation remain limited, especially with respect to three-dimensional fragment properties.

In recent years, additive manufacturing has attracted growing interest in the field of spacecraft shielding, as it enables the creation of complex, lightweight geometries that are difficult to achieve using conventional techniques. Experimental studies have shown that 3D-printed multilayer and composite configurations can improve resistance to hypersonic impacts, whilst offering greater flexibility in terms of design and production. These developments highlight the growing relevance of additively manufactured shielding solutions for next-generation spacecraft, particularly in the context of increasing orbital debris threats and the need for improved impact protection strategies [23–26].

In a previous study, the Space Debris Group of the University of Padova contributed to this body of work by conducting a series of hypervelocity impact tests on thin CFRP plates using spherical projectiles of 1.9 and 2.9 mm diameter at impact velocities between 3.5 km/s and 5.1 km/s [22]. The experimental campaign was carried out at the CISAS Hypervelocity Impact Facility using a two-stage Light-Gas Gun (LGG), capable of accelerating projectiles up to 100 mg at a maximum speed of 5.5 km/s [22,27–30]. The experiments were carried out above the ballistic limit, and the generated fragments were collected and analysed through a two-dimensional characterization, providing cumulative distributions of projected fragment dimensions. That study expanded the available experimental data toward higher impact velocities and larger thickness-to-diameter ratios compared to previous investigations. However, as commonly encountered in fragmentation studies, the absence of fragment mass and thickness measurements limited the possibility of deriving key parameters such as three-dimensional characteristic length, fragment volume, and A/m distributions.

The objective of the present work is to extend the analysis presented in Ref. [22] by performing a comprehensive three-dimensional characterization of all fragments generated during the CFRP impact experiments. Each fragment has been individually re-catalogued, weighed, and measured along its three principal axes, enabling the reconstruction of its three-dimensional geometry and the estimation of volume and area-to-mass ratio. This enhanced dataset allows the derivation of cumulative distributions of characteristic length and mass, as well as A/m-versus-size relationships and probability density functions of A/m. By providing detailed three-dimensional fragment information for CFRP targets, this study contributes new empirical data for the improvement of breakup models and long-term debris environment simulations, particularly for composite materials increasingly used in modern spacecraft.

The remainder of this paper is organized as follows. Section 2 describes the experimental setup and the methods. Section 3 focuses on fragments weight and geometric measurement. Section 4 presents the fragments analysis and the results in detail.

2. Experimental setup and methods

This section describes the origin of the fragments analysed and provides a concise overview of the experimental conditions under which they were generated.

The fragments examined in this study originate from four hypervelocity impact experiments conducted during a previous experimental campaign [22] at the CISAS Hypervelocity Impact Facility, using a two-stage Light-Gas Gun (LGG) system [28–30]. In all tests, aluminium (Al-1100) spheres were accelerated to hypervelocity and impacted on 10×10 cm^2 CFRP targets.

The test cases reported in Table 1 are characterised by comparable impact conditions in terms of target configuration and impact velocity, while differing in the type of projectile used. The resulting fragment populations cover a wide dimensional spectrum, ranging from fragments smaller than a millimetre to pieces with characteristic lengths of several millimetres, with corresponding masses distributed over several orders of magnitude. This wide dynamic range makes the dataset particularly suitable for statistical analysis and for studying correlations between geometric descriptors and physical properties.

After each test, once the fragments had been recovered from the Impact Facility Test Chamber, they were manually sorted into five size classes ($x > 3$ mm, $2 \text{ mm} < x < 3$ mm, $1 \text{ mm} < x < 2$ mm, $0.5 \text{ mm} < x < 1$ mm, and $x < 0.5$ mm), and the total mass of each class was subsequently measured [22]. For the sake of completeness, the results previously presented in Ref. [22] are reproduced here in Table 2.

While the experimental campaign reported in Ref. [22] offered a global statistical characterisation of the fragment populations, the present study expands that dataset by introducing a finer level of discretisation, an improved and more robust measurement chain, and a significantly higher measurement resolution. In particular, the correlation of the previously derived aggregate quantities with individual three-dimensional fragment measurements enables the mitigation of the morphological uncertainties associated with two-dimensional sampling approaches, thereby providing a deterministic framework for the evaluation of mass, characteristic length, and area-to-mass distributions.

It is noted that the analysis presented herein is restricted to fragments recovered in their entirety, whereas dust was excluded due to the

Table 1
Test set up and experimental data.

Test ID	Test number	Projectile diameter, mm	Projectile velocity, km/s	Projectile mass, g	Target thickness, mm	Target mass, g
T_BUM_11	9231	1.9	3.68	0.010	4	103.225
T_BUM_12	9227	1.9	5.10	0.010	4	100.489
T_BUM_13	9222	2.9	3.49	0.034	4	102.867
T_BUM_14	9224	2.9	4.63	0.034	4	100.767

Table 2
Total mass and number of detected fragments for each class.

Test ID	$L < 0.5$ mm		0.5 mm $< L < 1$ mm		1 mm $< L < 2$ mm		2 mm$<L < 3$ mm		$L > 3$ mm	
	Collected mass, g	N	Collected mass, g	N	Collected mass, g	N	Collected mass, g	N	Collected mass, g	N
T_BUM_11	0.028	1372	0.035	250	0.041	50	0.008	9	0.057	5
T_BUM_12	0.015	356	0.028	227	0.039	51	0.043	16	0	0
T_BUM_13	0.008	423	0.048	272	0.042	48	0.052	24	0.170	48
T_BUM_14	0.030	717	0.040	321	0.050	69	0.129	97	0.401	57

inherent impossibility of performing individual measurements. Nevertheless, the fragments that could not be individually characterised within each size class were weighed collectively to verify consistency between the total measured mass and the values reported in Table 2.

3. Fragment characterization methodology

In the initial stage of the measurement campaign, high-precision laboratory instrumentation was employed to enable the determination of fragment mass and geometric dimensions with sub-millimetre resolution. The main technical specifications of the balance and calliper used in the measurements are summarized in Table 3.

The balance was regularly re-zeroed in order to minimise the influence of residual environmental effects accumulated during successive measurements, and all weighing operations were performed under controlled conditions, free from air currents or drafts. Both the balance and the calliper were systematically cleaned with acetone to remove external contaminants, thereby ensuring measurement reliability and repeatability.

Using the high-precision instrumentation described above, the three principal dimensions (a, b, c) of each fragment were determined through direct measurements. Given the irregular morphology of the fragments, particular attention was devoted to defining a consistent orientation during the measurement process.

In this context, the RCC (Right Circular Cylinder)/REC (Right Elliptical Cylinder) representation, as used by NASA in the DebriSat project [31], was adopted solely as a geometrical reference to guide the identification of the fragment principal directions and is not used for the determination of the characteristic length.

For each fragment, the maximum dimension (a) was first identified as the largest measurable extent, as shown in Fig. 1. The fragment was then re-oriented to determine the intermediate dimension (b), orthogonal to a, and finally the minimum dimension (c), orthogonal to both a and b. This procedure provides a consistent bounding description of fragment geometry, suitable for irregular shapes.

These geometric parameters are subsequently employed to determine the characteristic length L_c:

$$L_c = \frac{a + b + c}{3} \tag{1}$$

Table 3
Main specifications of measuring instruments.

Characteristic	KERN ADB Balance	Mitutoyo Calliper
Resolution	10^{-4} g	0.01 mm
Capacity	220 g	150 mm

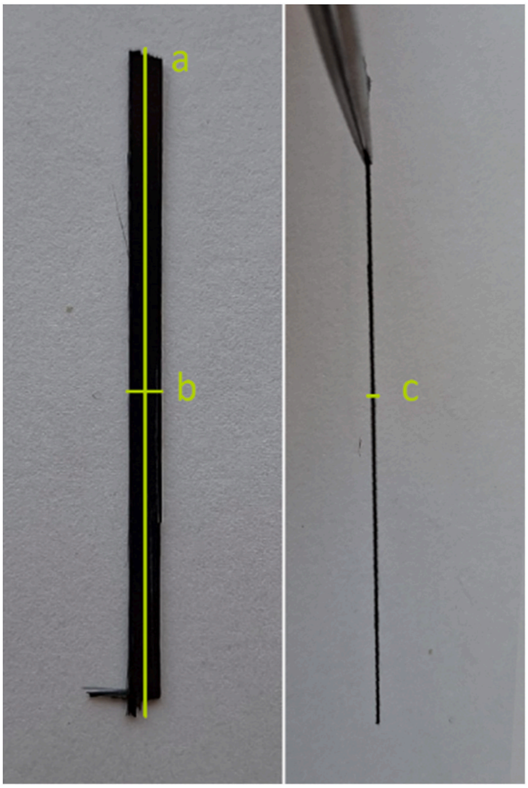

Fig. 1. CFRP fragment with definition of the principal dimensions (a, b, c).

This metric is adopted as the principal independent variable for the statistical distributions and scaling relationships examined in the following sections.

Each geometric dimension was measured multiple times using the digital calliper, and the corresponding arithmetic mean was taken as the representative value. Fragment mass was determined on an individual basis with the precision balance, with repeated weighings performed to improve repeatability and to reduce random measurement variability.

The overall measurement uncertainty was found to be predominantly governed by the instrumental resolution. Additional sources of variability related to manual handling and fragment orientation were effectively mitigated through repeated measurements and strict adherence to the RCC methodology.

Table 2 summarises the total collected mass and the number of detected fragments for each size class, as documented in Ref. [22]. The corresponding quantities for the subset of fragments individually characterised in the present study are reported in Table 4; for this analysis, only fragments with characteristic dimensions greater than 0.5 mm were considered. As discussed in Section 2, this subset also comprises fragments that could not be individually characterised geometrically and were therefore weighed collectively within each size class to preserve consistency and enable a direct comparison with the total mass values reported in Table 2 from the previous experimental campaign. For these aggregated subsets, the number of fragments was estimated through visual counting during the sorting process, while only the total mass could be measured. These fragments were assigned to the size classes defined during the previous experimental campaign [22], as their three-dimensional geometry could not be resolved on an individual basis.

The observed discrepancies can be mainly attributed to the substantially improved resolution of the balance employed in the present study, which increased by approximately one order of magnitude, from 10^{-3} g to 10^{-4} g. In addition, the availability of individual fragment measurements enabled a more accurate assignment to size classes compared with manual sifting, resulting in the reclassification of a limited number of fragments into smaller classes. Finally, the mass values reported here are obtained by summing the measurements of discrete fragments, thereby yielding a more precise characterisation than the class-averaged mass measurements adopted in the previous experimental campaign.

The cataloguing and measurement activities required approximately 82 h/person in total, corresponding to an average processing time of about 5 min/fragment, and were carried out by two operators. It is noted that the preliminary cataloguing of debris recovered from the firing chamber was not included in this estimate, as this task had already been completed during the previous analysis reported in Ref. [22].

4. Results

This section presents and discusses the main results, comparing the fragment distributions across the four experimental tests and through their corresponding average trends.

As outlined in Section 2, the statistical characterisation presented in this section is limited to fragments that were recovered in their entirety and individually measured in terms of mass and three-dimensional geometry. Fragments that could only be weighed collectively, owing to incomplete recovery or measurement constraints, were therefore excluded from the subsequent data analysis. The effective number of fragments considered in the analyses for each test and size class is reported in Table 5.

It should be noted that the size classes shown in Tables 2, 4 and 5 are based on the original classification obtained by sieving [22], whereas the distributions presented in this section are derived from the characteristic length L_c obtained through three-dimensional measurements. Due to the elongated morphology of the CFRP fragments, these two representations are not strictly equivalent and discrepancies may arise, particularly for thin fragments that may have passed through smaller sieve meshes despite having larger characteristic dimensions.

Table 5
Effective number of measured fragments for each class.

Test ID	0.5 mm < L < 1 mm	1 mm < L < 2 mm	2 mm<L < 3 mm	L > 3 mm
	N	N	N	N
T_BUM_11	110	48	0	0
T_BUM_12	118	35	13	0
T_BUM_13	183	42	21	41
T_BUM_14	159	69	75	48

4.1. Fragments characteristic length cumulative distributions

Fig. 2 illustrates the cumulative fragment number distributions as a function of the three-dimensional characteristic length L_c. A coherent trend is observed across the four experimental tests, while variations in fragment yield and distribution slope can be ascribed to differences in the respective experimental setups. A comparison with established fragmentation models, including the NASA Standard Breakup Model (SBM), reveals noticeable discrepancies in both the lower and upper fragment size classes, underscoring the strong dependence of fragment generation on projectile diameter, target thickness and impact parameters [10]. A significant portion of the debris generated is in the millimetre and submillimetre range, a size class that is particularly relevant for estimating untraceable debris populations. A comparison with the previously published two-dimensional fragment analysis in Ref. [22] indicates that the present three-dimensional results reproduce the main qualitative trends observed therein. In particular, the dependence of the cumulative fragment population on impact velocity and projectile diameter is confirmed: consistently with earlier findings, the number of fragments with characteristic length exceeding approximately 3 mm increases with both parameters, and this behaviour extends toward smaller fragment sizes as well. Furthermore, it should be noted that.

- Regarding the fragment size distributions, the earlier study reported a linear trend in the logarithmic reference frame for characteristic sizes below 2 mm, followed by a sudden decrease in the cumulative number and the onset of a second linear regime. In the present work, a full verification of the initial small-size linear trend is not possible, as fragments with $L_c < 0.5$ mm were not included in the analysis due to the resolution limits of the scale. Nevertheless, the presence of a pronounced intermediate drop in the cumulative distribution is clearly observed also in the three-dimensional analysis.
- This drop can be interpreted in a manner analogous to that proposed in the two-dimensional analysis, namely as the transition between fragments originating from the internal plies, whose dimensions are constrained by the crater size, and fragments generated by delamination of the external plies. In the present case, expressed in terms of the three-dimensional characteristic length, the transition occurs at $L_c \approx 2.3$ mm, while for the bidimensional analysis was $L_{c2} \approx 4$ mm.
- The dependence of the intermediate drop on impact energy is also preserved: as the impact velocity and projectile diameter increase, the drop becomes progressively less pronounced and is barely distinguishable for the most energetic configurations. This behaviour is consistent with an increasingly fine fragmentation of the delaminated region under more severe impact conditions.

Table 4
Total mass and estimated number of fragments for each class, including both individually characterised fragments and collectively weighed subsets.

Test ID	0.5 mm < L < 1 mm		1 mm < L < 2 mm		2 mm<L < 3 mm		L > 3 mm	
	Collected mass, g	N	Collected mass, g	N	Collected mass, g	N	Collected mass, g	N
T_BUM_11	0.0493	215	0.1138	48	0	0	0	0
T_BUM_12	0.0510	198	0.0726	35	0.0507	13	0	0
T_BUM_13	0.0514	183	0.0427	42	0.0419	21	0.1753	41
T_BUM_14	0.0811	320	0.0716	69	0.2110	75	0.4490	48

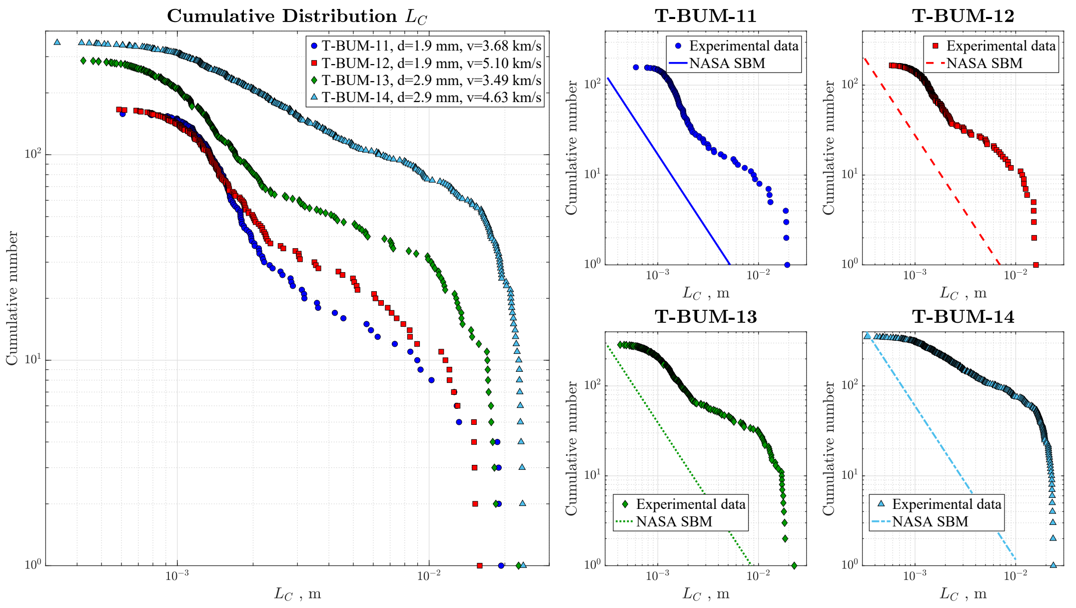

Fig. 2. Fragments cumulative number distributions in function of three-dimensional characteristic length L_c.

4.2. *Fragments mass distributions*

The distribution of fragments mass can be studied in relation to the three-dimensional characteristic length L_c; Fig. 3 reports the mass distributions for the four tests. It can be noted that tests conducted with larger diameter projectiles (tests 13 and 14) generate a higher number of fragments characterised by greater mass and larger L_c, in accordance with the trend already identified in the cumulative distributions of L_c. Conversely, tests performed with smaller diameter projectiles (tests 11 and 12) are mainly characterised by fragments with lower mass and reduced L_c. It should be noted that the horizontal alignment observed in several data points is due to the resolution limit of the scale.

As shown in Fig. 3, average distributions are also introduced by combining the data from all four tests to obtain an overall average curve (left) and by considering each test separately to obtain specific average curves for each (right). This approach allows for a clearer characterisation of the mass distribution of the fragments and its dependence on the characteristic length L_c. Furthermore, a piecewise linear regression was derived for the overall average curve, obtaining the following relationships with a breakpoint located at $\log_{10}(L_c) = -2.3$ ($L_c \approx 0.005$ m):

$$\log_{10}(m) = a_1 \log_{10}(L_c) + b_1, \log_{10}(L_c) \le -2.3 \tag{2}$$

$$\log_{10}(m) = a_2 \log_{10}(L_c) + b_2, \log_{10}(L_c) > -2.3 \tag{3}$$

Table 6
Parameters of the piecewise linear fit and corresponding R-squared value.

Regime	Coefficient a_i	Coefficient b_i	R^2
$\log_{10}(L_c) \le -2.3$	0.6816	−4.5378	0.9623
$\log_{10}(L_c) > -2.3$	1.6233	−2.3719	0.9749

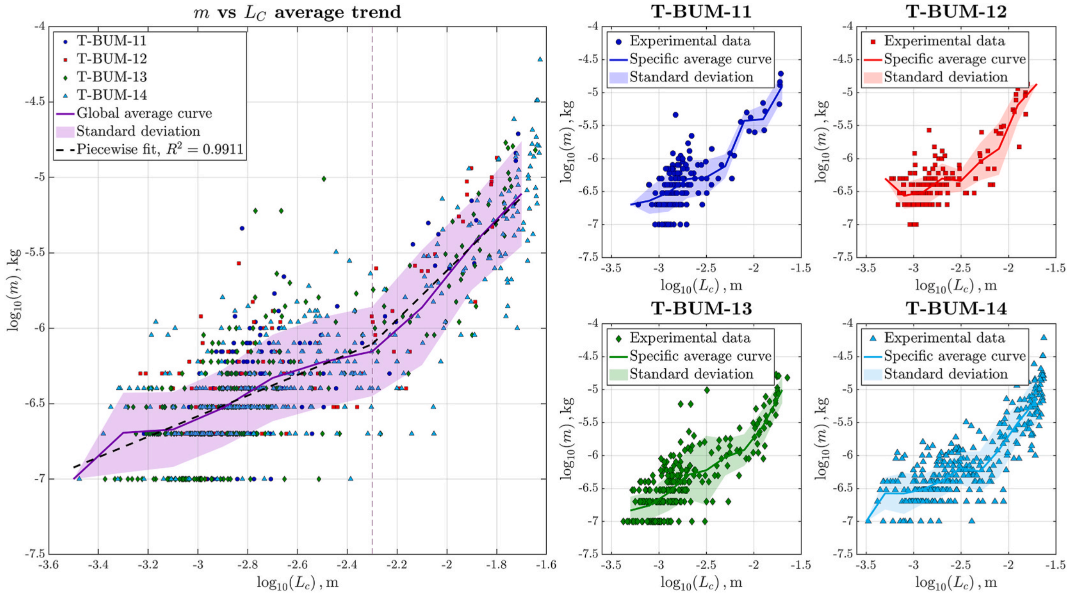

Fig. 3. Fragments mass distributions in function of L_c for all tests with the global average curve and standard deviation (left) and for each individual test with their specific average curves and standard deviations (right).

The slope and intercept values of the two regimes are summarized in Table 6, together with the corresponding coefficient of determination.

The average goodness of the fit is represented by an R-squared of 0.9911.

Table 7 reports the R-squared of the piecewise fit evaluated with respect to the global average curve, computed over different ranges of $\log_{10}(L_c)$.

The match between the global average curve and the specific average curves of the individual tests can be visually assessed in Fig. 4, where the latter are plotted alongside the global curve, represented by a dotted line. This representation allows for a direct evaluation of the extent to which the global trend reflects the behaviour of the individual tests.

A quantitative assessment of the goodness of the match between the global and specific average curves was defined as the root mean square error (RMSE), bias (intended as the average logarithmic vertical shift between global and specific average curves), and the coefficient of determination (R^2) R-squared.

The quantitative metrics reported in Table 8 indicate a good overall correspondence between the global average curves and the test-specific curves for all configurations considered. In particular, all tests show low RMSE values and coefficients of determination close to unity, indicating that the global average curve provides a representative description of the relationship between fragment mass and characteristic length within the adopted averaging framework. However, it is possible to identify a systematic dependence on the diameter of the bullet. Tests conducted with larger diameter bullets (tests 13 and 14) show the highest level of agreement, characterised by the lowest RMSE values and an R-squared greater than 0.97, while slightly higher, but still moderate, RMSE values and a marginally reduced R-squared are observed in tests with smaller diameter projectiles (tests 11 and 12). Although this trend may be influenced by the greater number of fragments generated in tests 13 and 14, which increases their statistical weight in the calculation of the global average curve, the relatively high R-squared values obtained for tests 11 and 12 indicate that the overall mean curve remains representative across all test conditions. The bias values further confirm this interpretation, revealing a systematic distinction between the two projectile diameter classes. Tests performed with smaller diameter projectiles (tests 11 and 12) are characterised by positive bias values, while those associated with larger diameter projectiles (tests 13 and 14) show a bias close to zero or slightly negative, indicating a closer alignment with the overall average curve. This behaviour reflects the influence of bullet diameter on the fragmentation process, while confirming that the overall average curve remains representative of the fragmentation behaviour across the entire set of parameters studied.

For completeness, the R-squared values between the global linear fit and the specific average curves are also reported in Table 9.

It should be noted that the global average curve presented in this section is obtained by binning the data with respect to the three-dimensional characteristic length L_c. This choice ensures consistency with the geometric characterization of the fragments and provides a stable representation of the relationship between fragment mass and characteristic length.

An alternative averaging approach, based on binning with respect to fragment mass, has also been investigated in order to assess the influence of measurement resolution effects. The corresponding results are reported in Appendix A, where a direct comparison between the two strategies is provided. The comparison highlights that the adopted L_c-based binning method is affected by the resolution limit of the balance, particularly in the low-mass regime. Due to the minimum detectable mass, fragments below the resolution threshold are not included in the dataset, resulting in a truncation of the fragment population at small characteristic lengths. As a consequence, the L_c-based method may lead to an under-representation of low-mass fragments and to a partial bias in the estimation of the mass-size relationship in this regime. While the mass-based averaging partially mitigates this effect for small fragments, it introduces increased variability at larger characteristic lengths. Therefore, the L_c-based approach has been retained as the primary methodology, as it provides a more robust and physically consistent representation of the overall trends. Nevertheless, the derived m vs L_c relationships should be interpreted with caution in the low-size regime, where measurement limitations affect the representativeness of the dataset. Their direct use for fragmentation model calibration may require careful consideration of these limitations, especially when extrapolating towards smaller fragment sizes.

Table 7
R-squared of the piecewise fit evaluated over different ranges of $\log_{10}(L_c)$, with respect to the global average curve.

Regime	R^2
$\log_{10}(L_c) < -3$	0.7753
$-3 \leq \log_{10}(L_c) \leq -2$	0.9510
$\log_{10}(L_c) > -2$	0.9900

4.3. Fragments area-to-mass distributions

The area-to-mass ratio is defined as the ratio between the cross-sectional area of the fragment and its mass. While mass is measured directly, area is estimated from the three-dimensional characteristic length of the fragment by applying the expressions provided in NASA's SBM model [10]:

$$A = 0.540424\, L_c^{\,2}, \text{ where } L_c < 0.00167\ m \tag{4}$$

$$A = 0.556945\, L_c^{\,2.047077}, \text{ where } L_c \geq 0.00167\ m \tag{5}$$

It should be noted that the cross-sectional area is estimated using an empirical formulation derived from the NASA Standard Breakup Model, which is based on datasets that do not fully represent the fragmentation behaviour of CFRP materials [10]. Due to the highly irregular morphology of composite fragments, significantly different cross-sectional areas may correspond to the same characteristic length. Experimental evidence available in the literature indicates that, for CFRP fragments, the A/m values associated with a given L_c may span up to two orders of magnitude [32]. As a result, the A/m values derived in this study should be interpreted as representative average estimates rather than exact geometric quantities, and a potentially significant variability due to fragment shape effects should be expected.

Fig. 5 presents the area-to-mass distributions obtained for each test together with the corresponding distributions studied in function of their size classes, i.e. for fragments between 0.5 mm and 1 mm (blue), between 1 mm and 2 mm (orange), between 2 mm and 3 mm (yellow) and larger than 3 mm (purple). The smaller classes are associated with lower $\log_{10}(A/m)$ values, generally close to 0 ÷ 0.5 (corresponding to 1 ÷ 3 m^2/kg), while the increase in fragment size leads to progressively higher values, approaching 1.5 ÷ 2 (30 ÷ 100 m^2/kg). This trend is further highlighted by the systematic shift to the right of each distribution peak as the size class increases, indicating an increase in the area-to-mass ratios for larger fragments.

Since the cross-sectional area of the fragments is approximately proportional to L_c^2, the observed increase in A/m with increasing characteristic length suggests that the area of the fragments grows faster than the mass as the size increases, implying that larger fragments are proportionally less massive. It should be noted, however, that this trend may be partially influenced by the resolution limit of the balance, particularly in the low-mass regime. This trend is further supported by the global mass-size relationship derived in Section 4.2, where the piecewise linear fit of the global average curve (Eqs. (2) and (3)) indicates that $m \, \alpha \, L_c^{0.6816}$ in the lower regime and $m \, \alpha \, L_c^{1.6233}$ in the higher regime, implying $m \, \alpha \, L^{\delta}$ where $0 < \delta < 2$. Since the cross-sectional area is evaluated following NASA's SBM (Eqs. (4) and (5)), with a maximum

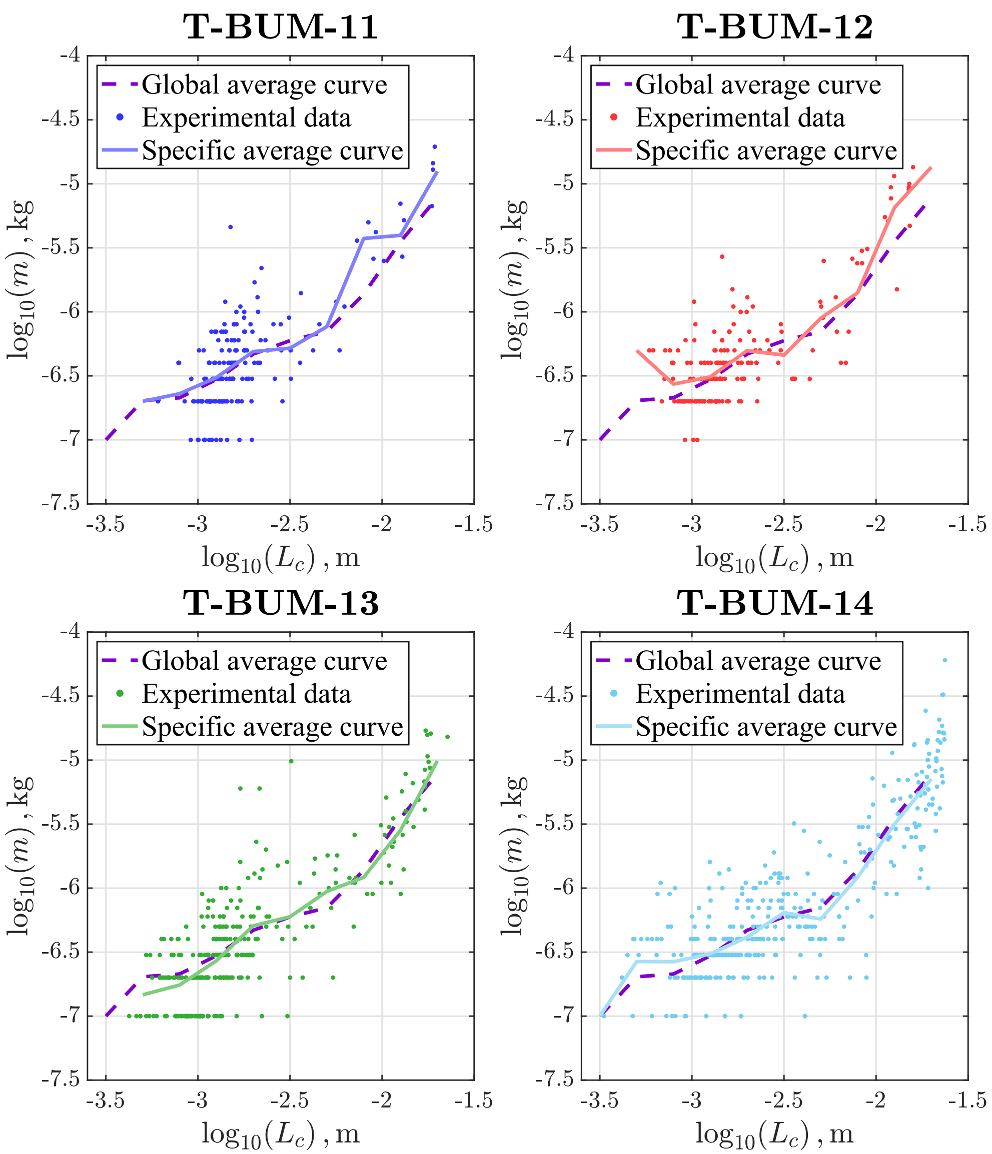

Fig. 4. Specific average curves of fragments mass distribution versus L_c compared with the global average curve.

Table 8
RMSE, bias and R^2 for global vs specific m vs L_c average curves (common range).

Test ID	RMSE	Bias	R^2
T_BUM_11	0.1634	0.0808	0.9257
T_BUM_12	0.1877	0.1168	0.8883
T_BUM_13	0.0873	−0.0168	0.9753
T_BUM_14	0.0651	−0.0020	0.9845

Table 9
R^2 for global linear fit vs specific m vs L_c average curves (common range).

Test ID	R^2
T_BUM_11	0.9397
T_BUM_12	0.8562
T_BUM_13	0.9739
T_BUM_14	0.9639

dependence of $A\ \alpha\ L_c^{2.047077}$, it follows that $A/m\ \alpha\ L_c^{\gamma}$ with $\gamma > 0$, consistent with the observed increase of $log_{10}(A/m)$ with increasing fragment size. Overall, the resulting distributions show that fragment size strongly influences the area-to-mass ratio, with smaller fragments being relatively dominated by mass and larger fragments increasingly dominated by area.

A similar analysis is also performed by grouping the fragments from all four tests in order to obtain an overall area-to-mass distribution, shown in Fig. 6. The resulting distribution shows that most fragments fall within the range $-0.5 \leq log_{10}(A/m) \leq 1.5$, corresponding to area-to-mass ratios between approximately 0.3 and 30 m^2/kg, reflecting the predominance of fragments with intermediate area-to-mass ratios in the overall population. In line with the trends observed in Fig. 5, the peak of the distributions progressively shifts towards higher log10(A/m) values as the size class increases, confirming also at a global level that larger fragments are characterised by higher area-to-mass ratios and are therefore proportionally less massive.

4.4. Fragments area-to-mass vs characteristic length distributions

Fig. 7 shows the area-to-mass distribution as a function of the three-dimensional characteristic length L_c. There is a marked concentration of fragments in the range $-0.5 \leq log_{10}(A/m) \leq 1.5$, in line with section 4.3; these fragments correspond to $log_{10}(L_c)$ values between −3.4 and −1.6 (0.39 mm < L_c < 25 mm). Fragments from tests performed with larger

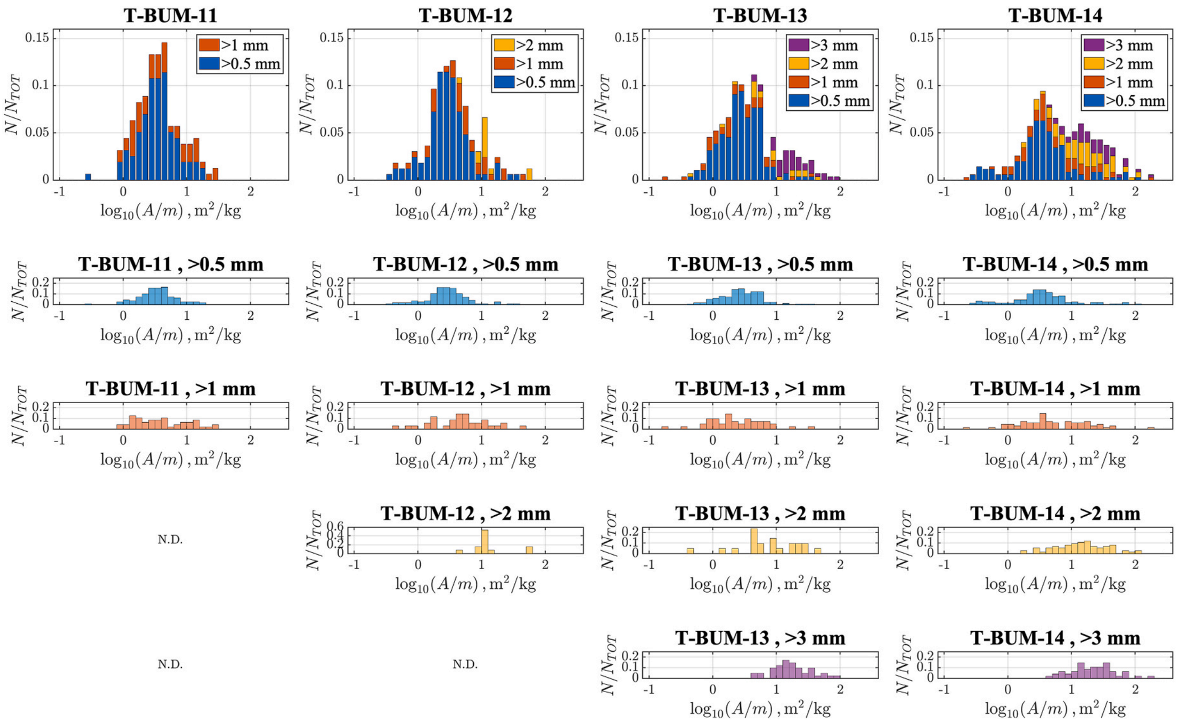

Fig. 5. Area-to-mass distributions for each test (top) and for the corresponding fragment size classes (bottom). (N.D. – not determinable).

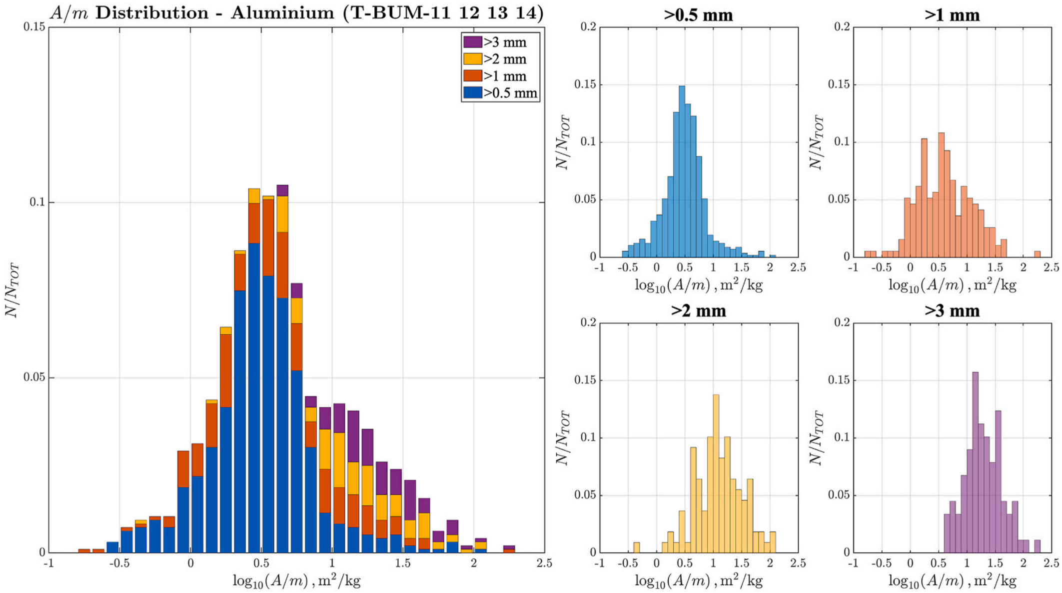

Fig. 6. Global area-to-mass distributions for all tests (left) and for the corresponding fragment size classes (right).

diameter projectiles (tests 13 and 14) extends towards higher L_c values, reflecting the generation of larger fragments under these impact conditions. The graph further confirms the behaviour discussed in Section 4.3: since the cross-sectional area of the fragments is approximately proportional to L_c^2, the observed increase in A/m with increasing characteristic length indicates that the area of the fragments increases faster than the mass as the size increases, implying that larger fragments are proportionally less massive. It should be noted that the diagonal alignment observed in several data points is due to the resolution limit of the scale. In the low-mass regime, fragments with masses close to the detection threshold cannot be measured accurately, whilst those with even lower masses are not detected at all. Consequently, for small characteristic lengths, only fragments with relatively higher masses are included in the dataset, whilst those with lower masses are systematically excluded, as they are not detected by the scale. Since these excluded fragments would correspond to higher A/m values, their absence produces a one-sided truncation of the distribution. This leads to an apparent shift of the A/m vs L_c distribution towards lower values and an increasing bias as fragment sizes decrease. Consequently, the average trends derived in the low L_c region should be interpreted with caution, as they may not fully represent the underlying fragment population.

Similar to the procedure adopted for mass distributions in function of L_c, average curves are also introduced for area-to-mass distributions vs

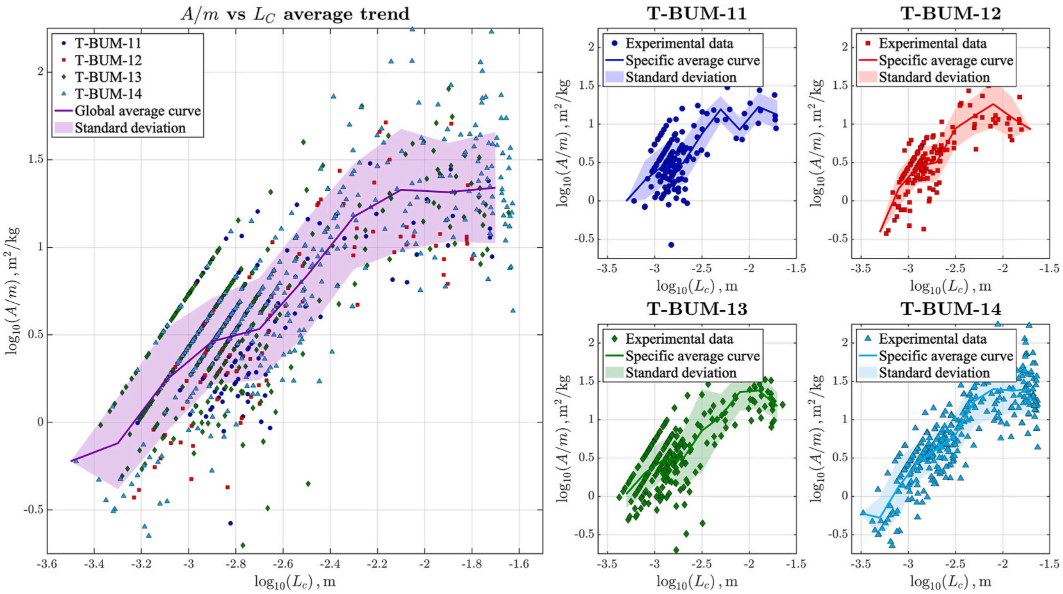

Fig. 7. Fragments area-to-mass distributions in function of L_c for all tests with the global average curve and standard deviation (left) and for each individual test with their specific average curves and standard deviations (right).

L_c, considering both all tests together (global average) and each test separately (specific averages). The resulting average curves show a clear upward trend as L_c increases, further confirming that the increase in A/m is intrinsically linked to the size of the fragments and reflects the predominance of area growth over mass as the size of fragments increases.

The agreement between the overall average curves and those specific to each test is assessed visually in Fig. 8, where each specific curve is compared with the overall curve shown as a dotted line. A quantitative evaluation of their correspondence is carried out using RMSE, bias (mean logarithmic vertical displacement) and R-squared, reported in Table 10.

The statistical metrics highlight a good overall match between the global and specific average curves for all cases. All tests are characterised by moderate to low RMSE values and R-squared well above 0.84, indicating that the global average curve provides a consistent representation of the area-to-mass vs characteristic length trend across the entire dataset. However, a systematic dependence on projectile diameter can be identified as tests performed with larger projectile diameter (tests 13 and 14) show the highest level of correspondence, with lowest RMSE values and R-squared values greater than 0.95, while tests with smaller projectile diameter (tests 11 and 12) show slightly higher RMSE values and marginally reduced R-squared values.

The bias values further confirm this interpretation, remaining low in all tests and indicating only limited systematic deviations from the overall average curve. Tests with smaller diameter projectiles are associated with slightly negative bias values, while those with larger diameter projectiles have bias values close to zero. Overall, these results suggest that the area-to-mass scaling behaviour in CFRP fragmentation is well represented by a single global trend in the set of parameters studied, with the projectile diameter mainly influencing the degree of dispersion rather than inducing distinct fragmentation regimes.

It is important to highlight that the global average curve presented in this section is derived by grouping the data according to the three-dimensional characteristic length L_c. An alternative approach, based on grouping the data by fragment mass, has also been explored to evaluate the impact of measurement resolution effects. The results obtained with this method are presented in Appendix A, where a direct comparison between the two approaches is provided.

5. Conclusions

This work presented the results of an experimental investigation of the fragmentation generated by perforation tests on Carbon-Fiber-Reinforced Composite Panels targets 4 mm thick, struck by spherical aluminium projectiles with a diameter of 1.9 mm and 2.9 mm at velocities between 3.5 and 5.1 km/s. The dimensions and masses of the fragments were systematically measured and catalogued, allowing cumulative distributions of characteristic length, mass distributions, area-to-mass distributions and area-to-mass distributions as a function of characteristic length to be obtained.

The cumulative distributions of characteristic lengths indicate that most fragments fall within the millimetre and submillimetre range, with fragment size and population strongly influenced by bullet diameter and impact velocity. Consistently, the mass distributions show that tests performed with larger diameter projectiles (tests 13 and 14) produce larger and more massive fragments, while configurations involving smaller projectiles (tests 11 and 12) are dominated by lighter and smaller debris. The area-to-mass distributions showed that smaller fragments are associated with low A/m ratios, close to 0.3 m^2/kg, while the increase in fragment size leads to progressively higher ratios, approaching 30 m^2/kg, confirming that the area of the fragments grows faster than the mass as the characteristic length increases. The analysis of area-to-mass ratio versus L_c further support the same trend, with global and specific average curves showing strong agreement for tests performed with larger projectile diameter and only minor deviations for tests with smaller projectile diameter, quantified by RMSE, bias, and R-squared.

Overall, the results indicate that the properties of the fragments depend largely on the projectile diameter and the impact conditions, while the global scaling laws provide an appropriate description of the fragmentation trends in all the configurations investigated.

These results provide a quantitative framework for predicting fragment characteristics and can support the development of protective materials, impact mitigation strategies, and debris assessment methodologies in aerospace applications.

The methodology adopted in this study can be extended to a broader range of impact scenarios, including different material systems, target thicknesses, and impact conditions, providing a consistent framework for the three-dimensional characterization of fragment populations. In

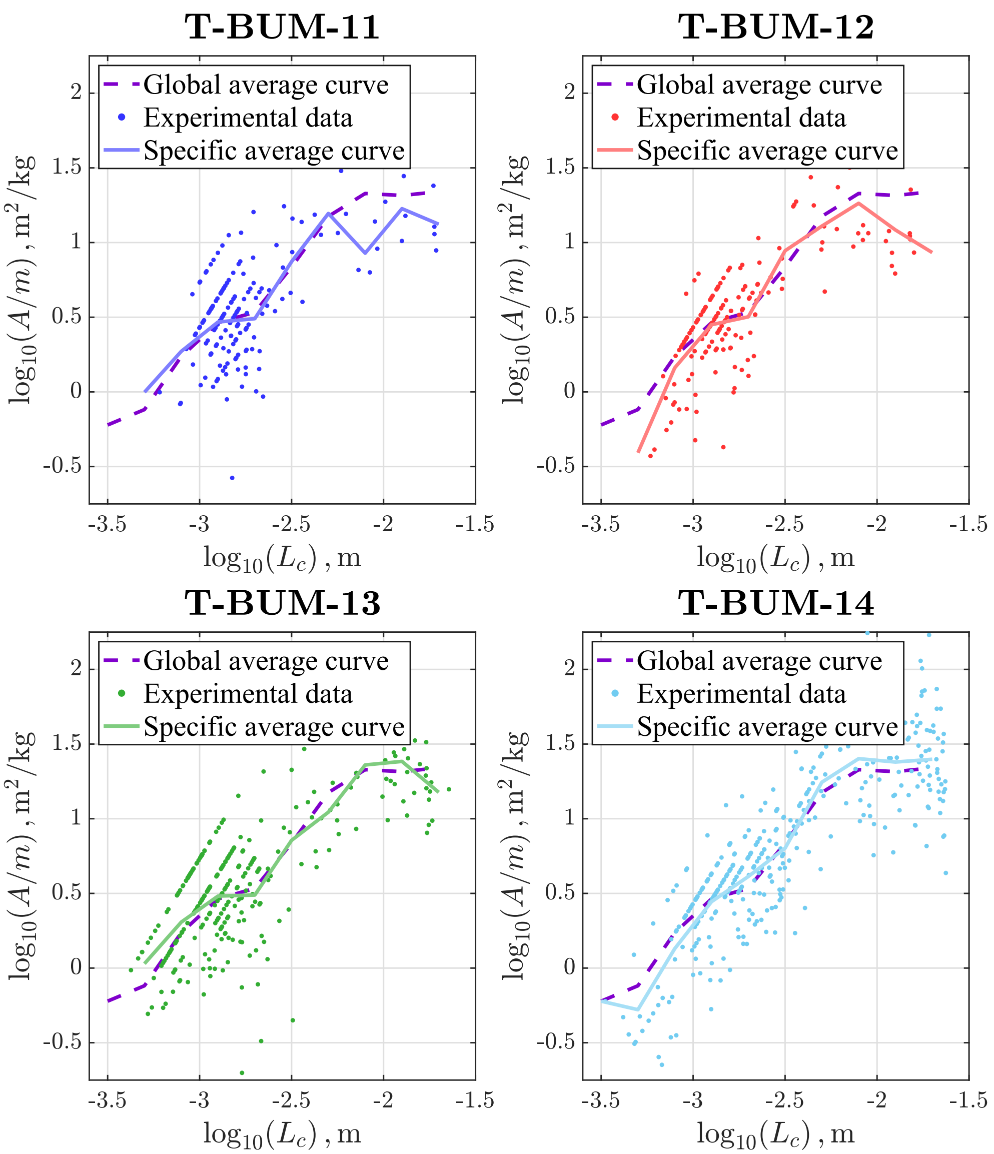

Fig. 8. Specific average curves of fragments area-to-mass distribution versus L_c compared with the global average curve.

Table 10
RMSE, bias and R^2 for global vs specific A/m vs L_c average curves (common range).

Test ID	RMSE	Bias	R^2
T_BUM_11	0.1610	−0.0599	0.8494
T_BUM_12	0.1918	−0.1190	0.8597
T_BUM_13	0.0940	0.0019	0.9580
T_BUM_14	0.0796	0.0024	0.9842

particular, its application to other composite materials and hybrid structures may contribute to improving the representativeness of current fragmentation models.

It should also be noted that the estimation of the area-to-mass ratio is based on an empirical formulation derived from the NASA Standard Breakup Model, which may not fully capture the variability of CFRP fragment shapes [10]. As reported in the literature, fragments with similar characteristic length may exhibit *A/m* values differing by up to two orders of magnitude [32]. Therefore, the *A/m* trends presented in this work should be interpreted as representative average behaviours, and a significant variability due to fragment shape effects should be expected.

Future work will focus on expanding the experimental dataset to different impact configurations and material types, as well as integrating the obtained results into existing breakup models to enhance their predictive capabilities. Further developments may also include the refinement of measurement techniques and the investigation of fragment morphology and shape effects, in order to better capture the physical mechanisms governing fragmentation under hypervelocity impact conditions.

CRediT authorship contribution statement

Francesco Fabri: Writing – original draft, Visualization, Validation, Investigation, Formal analysis, Data curation. **Lorenzo Olivieri:** Writing – review & editing, Validation, Supervision, Methodology, Formal analysis, Data curation, Conceptualization.

Declaration of competing interest

The authors declare that they have no known competing financial interests or personal relationships that could have appeared to influence the work reported in this paper.

Acknowledgments

This work has been supported by the Italian Space Agency in the framework of the agreement n.2023-37-HH.0 “Attività tecnico-scientifiche di supporto a C-SSA/ISOC”. The hypervelocity impact experiments cited in this work were performed in the framework of ESA contract n. TDE-T711–603SD “Exploiting numerical modelling for the characterisation of collision break-ups”. The authors wish to thank Mr. Marco Lazzarato and Mr. Alessio Vianello for the support in fragments measurement activities.

Appendix A

In order to assess the influence of the binning strategy on the derived scaling relationships, additional analyses were performed using a mass-based averaging approach. In this case, the data were grouped according to fragment mass, and the corresponding average values of L_c and A/m were computed for each bin.

Figure A1 and Figure A2 compare the results obtained using mass-based and L_c-based binning method for the global average curves.

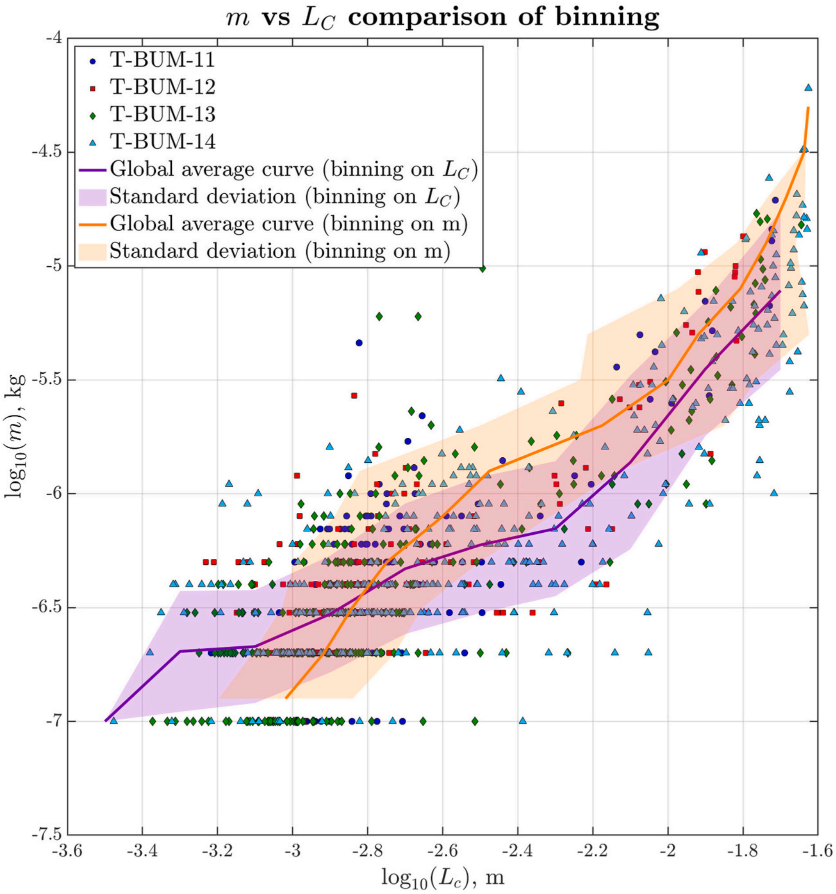

Fig. A1. Comparison of the binning methods for global average curve of the mass distribution in function of L_c for all tests.

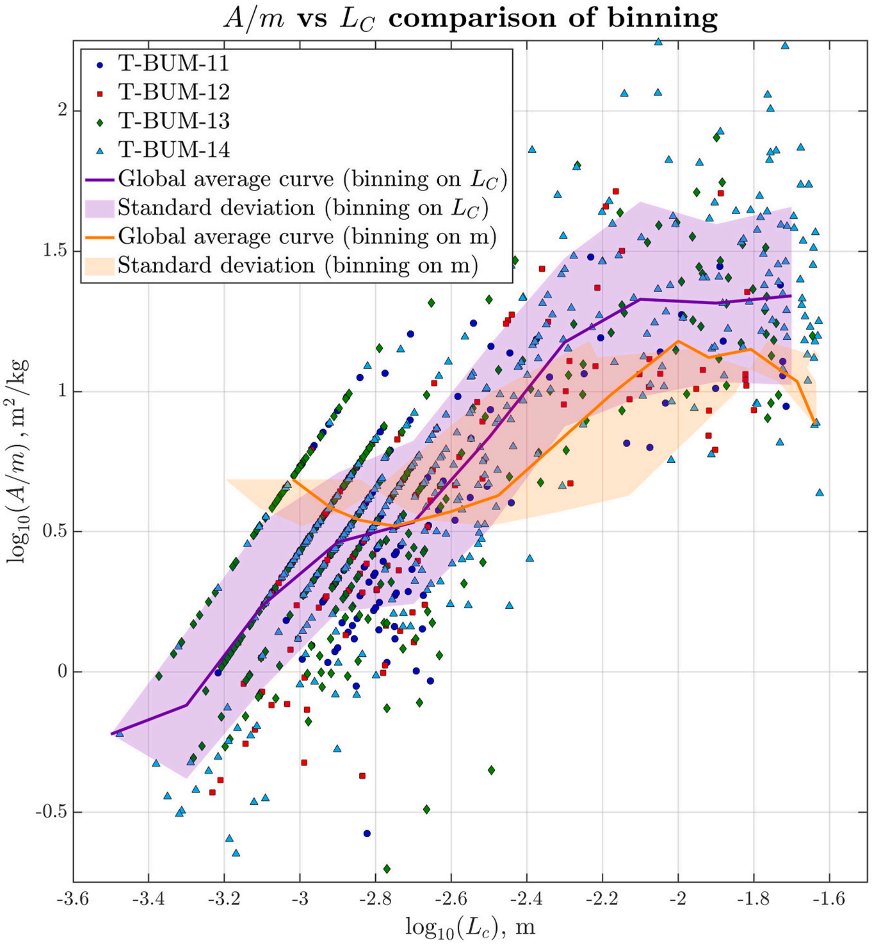

Fig. A2. Comparison of the binning methods for global average curve of the area-to-mass distribution in function of L$_c$ for all tests.

The comparison highlights a systematic difference between the two averaging strategies. In the low characteristic length regime ($L_c \lesssim 5$ mm), the mass-based binning provides a smoother and more consistent trend. This behaviour can be attributed to the resolution limit of the balance, which introduces a truncation in the measurable mass range. Therefore, binning with respect to L_c leads to a discretisation effect and an under representation of low-mass fragments, while mass-based binning partially mitigates this issue.

Conversely, in the higher characteristic length regime, the L_c-based binning method shows a more stable and physically consistent behaviour. In this region, the dataset is not affected by mass resolution limitations, and the grouping based on L_c preserves the geometric consistency of the fragment population. On the other hand, mass-based binning introduces increased dispersion and less stable trends, particularly due to the reduced number of fragments at larger sizes.

These observations confirm that the two approaches provide complementary insights into the fragment scaling behaviour. While mass-based binning method is more suitable for analysing the low-size regime affected by measurement limitations, the L_c-based approach adopted in the main analysis provides a more robust representation of the overall scaling trends and has been therefore retained as the reference methodology in this work.

References

[1] D.J. Kessler, B.G. Cour-Palais, Collision frequency of artificial satellites: the creation of a debris Belt, J. Geophys. Res.: Space Phys. 83 (A6) (1978) 2637–2646.
[2] D.J. Kessler, N.L. Johnson, J.-C. Liou, M. Matney, The kessler syndrome: implications to future space operations, Adv. Astronaut. Sci. 137 (2010).
[3] B. Cour-Palais, Hypervelocity impacts in space, Acta Astronaut. 10 (1) (1983) 11–24.
[4] H. Klinkrad, Space Debris – Models and Risk Analysis, Springer, 2006.
[5] R. Putzar, F. Schäfer, Damage to spacecraft structures by hypervelocity impacts, Int. J. Impact Eng. 35 (12) (2008) 1697–1703.
[6] L. Olivieri, A. Francesconi, Large constellations assessment and optimization in the LEO debris environment, Adv. Space Res. 65 (1) (2020) 351–363.
[7] H. Lewis, J. Radtke, A. Rossi, J. Beck, M. Oswald, P. Anderson, B. Bastida Virgili, H. Krag, Sensitivity of the space debris environment to large constellations, J. Br. Interplanet. Soc. (JBIS) 70 (2017) 105–117.
[8] J.C. Dolado-Perez, C. Pardini, L. Anselmo, Review of uncertainty sources affecting long-term space debris predictions, Acta Astronaut. 113 (2015) 51–65.
[9] Inter-Agency Space Debris Coordination Committee, IADC Space Debris Mitigation Guidelines, 2007.
[10] N.L. Johnson, P.H. Krisko, J.-C. Liou, P.D. Anz-Meador, NASA's new breakup model of EVOLVE 4.0, Adv. Space Res. 28 (9) (2001) 1377–1384.
[11] P.H. Krisko, M. Hostman, M.L. Fudge, SOCIT-4 collision breakup data analysis, Adv. Space Res. 41 (2008) 1138–1146.
[12] J.-C. Liou, S. Clark, N. Fitz-Coy, T. Huynh, J. Opiela, M. Polk, B. Roebuck, R. Rushing, M. Sorge, M. Werremeyer, DebriSat - a planned laboratory-based satellite impact experiment for breakup fragment characterization, Proc. 6th European Conference on Space Debris, ESA (2013).
[13] H. Cowardin, P. Anz-Meador, J. Murray, J.-C. Liou, E. Christiansen, M. Sorge, N. Fitz-Coy, T. Huynh, Updates to the DebriSat project in support of improving breakup models and orbital debris risk assessments. Hypervelocity Impact Symposium, ASME, 2019.
[14] T. Hanada, J.-C. Liou, Comparison of fragments created by Low- and hypervelocity impacts, Adv. Space Res. 41 (7) (2008) 1132–1137.
[15] S. Lan, S. Liu, Y. Li, F. Ke, J. Huang, Debris area distribution of spacecraft under hypervelocity impact, Acta Astronaut. 105 (2014) 75–81.

[16] M. Nishida, H. Kato, K. Hayashi, M. Higashide, Ejecta size distribution resulting from hypervelocity impact of spherical projectiles on CFRP laminates, Procedia Eng. 58 (2013) 533–542.

[17] M. Nishida, A. Hongo, Y. Hiraiwa, M. Higashide, Effects of gamma ray irradiation on penetration hole in and fragments size from carbon fiber reinforced composite plates in hypervelocity impacts, Compos. B Eng. 169 (2019) 229–238.

[18] M. Nishida, K. Hayashi, M. Higashide, Effects of projectile diameter and specimen thickness on size distribution of ejecta resulting from carbon fiber reinforced plastic plates in hypervelocity impacts, Journal of the Society of Material Science, Japan 67 (4) (2018) 445–451.

[19] M. Nishida, A. Hongo, H. Takahara, M. Higashide, Effects of electron beam irradiation on hypervelocity imact behavior of carbon fiber reinforced plastic plates, J. Compos. Mater. 55 (29) (2021) 4295–4304.

[20] A. Francesconi, C. Giacomuzzo, S. Kibe, Y. Nagao, M. Higashide, Effects of high-speed impacts on CFRP plates for space applications, Adv. Space Res. 50 (5) (2012) 539–548.

[21] M. Higashide, T. Kusano, Y. Takayanagi, K. Arai, S. Hasegawa, Comparison of aluminum alloy and CFRP bumpers for space debris protection, Procedia Eng. 103 (2015) 189–196.

[22] L. Olivieri, C. Giacomuzzo, A. Francesconi, Analysis of fragment distributions from carbon-fiber-reinforced composite panels subjected to hypervelocity impacts, AIAA J. (2023).

[23] J. Boudrie, E. Shea, H. Pyzdrowsky, K. Brisker, P. Fiori, M.L. Anderson, J. Rausch, P.T. Mead, K.R. Kota, T.E. Lacy, Design and Evaluation of Additively-Manufactured MMOD Satellite Shielding, AIAA SCITECH 2023 Forum, 2023.

[24] S. Lopresti, L. Barilaro, A. Abiti, L. Olivieri, Rapid prototyping of satellite shields: 3D printed carbon fiber and kevlar composites for hypervelocity impact protection, Acta Astronaut. (2025).

[25] S.W. Paek, S. Balasubramanian, D. Stupples, Composites additive manufacturing for space applications: a review, Materials 15 (2022) 4709, https://doi.org/10.3390/ma15134709.

[26] L. Olivieri, C. Giacomuzzo, A. Francesconi, H. Stokes, A. Rossi, Experimental characterization of multi-layer 3D-printed shields for microsatellites, Journal of Space Safety Engineering (2020).

[27] L. Olivieri, C. Giacomuzzo, A. Francesconi, Experimental fragments distributions for thin aluminium plates subjected to hypervelocity impacts, Int. J. Impact Eng. 170 (2022) 104351.

[28] F. Angrilli, D. Pavarin, M. De Cecco, A. Francesconi, Impact facility based upon high frequency two stage light-gas gun, Acta Astronaut. 53 (3) (2023) 185–189, https://doi.org/10.1016/S0094-5765(02)00207-2.

[29] D. Pavarin, A. Francesconi, Improvement of the CISAS high-shot frequency light-gas gun, Int. J. Impact Eng. 29 (1–10) (2024) 549–562, https://doi.org/10.1016/j.ijimpeng.2003.10.004.

[30] A. Francesconi, D. Pavarin, A. Bettella, F. Angrilli, A special design condition to increase the performance of two-stage light-gas guns, Interntional Journal of Impact Engineering 35 (12) (2008) 1510–1515, https://doi.org/10.1016/j.ijimpeng.2008.07.035.

[31] H. Cowardin, E. Christiansen, M. Matney, J. Miller, B. Davis, C. Cruz, J. Seago, A. King, J. Opiela, A. Manis, Orbital debris shape effect investigations for mitigating risk, J. Astronaut. Sci. 71 (6) (2024) 49.

[32] J. Murray, H. Cowardin, J.-C. Liou, M. Sorge, N. Fitz-Coy, T. Huynh, Analysis of the Debrisat Fragments and Comparison to the NASA Standard Satellite Breakup Model, First International Orbital Debris Conference, 2019.